



## Supporting Online Material for

### **Large-Scale Controls of Methanogenesis Inferred from Methane and Gravity Spaceborne Data**

A. Anthony Bloom, Paul I. Palmer,\* Annemarie Fraser, David S. Reay, Christian Frankenberg

\*To whom correspondence should be addressed. E-mail: pip@ed.ac.uk

Published 15 January 2010, *Science* **327**, 322 (2010)

DOI: 10.1126/science.1175176

**This PDF file includes:**

SOM Text  
Figs. S1 to S6  
Table S1  
References

# 1 Supporting online material for Large-scale Controls of Methanogenesis Inferred From Methane and Gravity Spaceborne Data by Bloom, Palmer, Fraser, Reay and Frankenberg

## 1.1 SCIAMACHY CH<sub>4</sub> columns

5 We use satellite column observations of CH<sub>4</sub> from the SCanning Imaging Absorption spectroMeter for Atmospheric CHartographyY (SCIAMACHY) instrument (1), aboard ENVISAT, which have been retrieved from solar-backscattered radiation at 1630–1679 nm wavelengths (2), accounting for new water spectroscopic parameters (3). Retrieved columns, most sensitive to CH<sub>4</sub> in the lower troposphere (2), range from 1630 ppb to 1810 ppb, with the largest values generally over midlatitude and tropical continents (3). The data consist of CH<sub>4</sub> and CO<sub>2</sub> Vertical Column Densities (VCD) during January 2003 to October 2005 (2).

15 The SCIAMACHY pixel size for CH<sub>4</sub> VCD is 30 km by 120 km while for CO<sub>2</sub> VCD it is 30 km by 60 km (4). Although the SCIAMACHY swath is discontinuous along its track, the gaps are filled by subsequent orbits and near-global coverage can be achieved within 7 days. The exclusion of unreliable data, such as measurements over oceans and during cloudy conditions, results in substantial coverage gaps.

The mean column volume mixing ratio (CVMR) of CH<sub>4</sub> within the atmospheric column has been derived using equation 1

$$CH_4^{CVMR} = \left( \frac{CH_4^{VCD}}{CO_2^{VCD}} \right) CO_2^{CVMR}, \quad (1)$$

20 where  $CH_4^{VCD}$  and  $CO_2^{VCD}$  are the vertical column densities of CH<sub>4</sub> and CO<sub>2</sub>, and  $CO_2^{CVMR}$  is the mean column volume CO<sub>2</sub> mixing ratio. We derive  $CH_4^{CVMR}$  using mean values of  $CO_2^{CVMR}$  obtained from the global CarbonTracker model (5). The  $CH_4^{VCD}$  data is then interpolated onto a  $3^\circ \times 3^\circ$  grid.

## 1.2 GRACE data

The Gravity Recovery and Climate Experiment (GRACE) mission consists of a twin satellite system that measures the temporal change in the Earth’s gravitational field. Global coverage by the satellite is achieved every 30 days (6), although the effective temporal resolution is equivalent to 10 days with a maximum resolution of 400 km (7). The global gravity field is described as a geoidal height, the deviation of the gravitational equipotential surface from a reference, Earth geoid, in spherical harmonics. Equivalent water height,  $\Gamma$ , can be derived as a weighted sum of the geoid spherical harmonics with respect to spherical degree and the Earth’s load deformation coefficients (8). We use the CNES 10 day  $1^\circ \times 1^\circ$  groundwater equivalent product  $\Gamma$  with an effective resolution of 667 km (8) which we interpolate to a  $3^\circ$  by  $3^\circ$  grid.

### 1.3 NCEP/NCAR surface temperature data

We used surface skin temperature ( $T_s$ ), the temperature of the surface at radiative equilibrium, from NCEP/NCAR re-analysis data (9) as a proxy for soil temperature. We chose to use skin temperature because subsurface temperature estimates may contain additional model error (10) and the three-layer soil temperature model used in the NCEP/NCAR re-analysis (9) is not globally representative of wetland temperature regimes due to the variable wetland depths. Over 2003–2007, we find that NCEP/NCAR  $T_s$  value reproduce 97% of the variability of soil temperature at 10 cm depth in ice free regions; the range of soil temperatures is smaller than the range of surface skin temperatures, which leads to a small underestimate of inferred  $Q_{10}(T_0)$ .

Surface skin temperature fields are derived from T62 Gaussian grid NCEP re-analysis fields at a temporal resolution of 6 hours. The average grid resolution within latitudes of 60°S and 60°N is approximately 2°. The data was then interpolated to a 3° × 3° resolution. NCEP/NCAR  $T_s$  fields agree with satellite data to a level consistent with the 40-year ECMWF reanalysis (11).

### 1.4 GEOS-Chem chemistry transport model of CH<sub>4</sub>

We use the GEOS-Chem 3-D global chemical transport model (version v8-01-01), driven by version 4 of the assimilated meteorological fields from NASA’s Global Modeling and Assimilation Office. For this study we run the model at a horizontal resolution of 2° × 2.5°, with 30 vertical levels. We include anthropogenic sources of CH<sub>4</sub> from ruminant animals, coal mining, oil production, landfills (12); biomass burning (13); and biofuel burning (14). We include natural sources from termites and hydrates, and a soil sink (15). Emissions from rice and wetlands were either taken from bottom-up inventories (15) or based on results from our study. We use monthly mean 3-D OH fields (16) to describe the tropospheric OH sink of CH<sub>4</sub>. Loss rates for CH<sub>4</sub> in the stratosphere were adapted from a 2-D stratospheric model (17).

### 1.5 The relationship between wetland emissions and CH<sub>4</sub> columns

We use the GEOS-Chem model to characterise the relationship between wetland emissions (15) and CH<sub>4</sub> columns. We run the model for a complete year and analyse daily output. We sample the model between 10-12 local time, the approximate overpass time of ENVISAT. To account for vertical sensitivity of SCIAMACHY we apply a mean instrument averaging kernel to model profiles of CH<sub>4</sub> and vertically integrate the resulting profile to obtain columns. The model columns and wetland emissions were averaged over 10-day periods to be consistent with our data analysis.

We calculate grid point correlations ( $r^2$ ) between model columns and monthly-varying emissions of rice and wetlands. Figure 1 shows that  $r^2$  correlations are typically >0.7 where bottom-up emission estimates locate rice paddies and wetlands, supporting the idea that variability of these surface emissions determine variability of overlying CH<sub>4</sub> columns. Correlations between model CH<sub>4</sub> columns and integrated OH columns are an order of magnitude less than with rice or wetlands, and spatially more diffuse.

For each grid point, we also calculate the gradient between the peak-to-peak amplitude of wetland and rice paddy emissions and overlying CH<sub>4</sub> columns using a least-squares estimation method (18).

We assign a 5% error to the model columns, representing the maximum difference between the model and surface flask measurements. No error was assigned to the emissions. The gradient given here is the global mean with its standard error:  $1.9 \pm 0.3$  (ppb/(mg/m<sup>2</sup>/day)),  $n=1828$  for rice+wetlands. Individual gradients more than three standard deviations from the mean were omitted, eliminating grid points with very small emission variation.

## 1.6 Estimating changes in CH<sub>4</sub> due to seasonal variations in OH sink

We use monthly mean tropospheric OH concentrations calculated using the GEOS-Chem chemistry and aerosol simulation (16) to determine the annual variability of CH<sub>4</sub><sup>VMR</sup> due to changes in oxidation by the OH radical.

We estimate the change in CH<sub>4</sub> concentrations due to seasonal variations of OH by subtracting the loss of CH<sub>4</sub> due to the annual mean OH concentration (ppb/month) from CH<sub>4</sub> loss due to monthly mean OH concentrations (ppb/month) and integrating the residual over a year:

$$[CH_4^{OHcor}] = \int \frac{d[CH_4^{OHloss}]}{dt} - \frac{\overline{d[CH_4^{OHloss}]}}{dt} dt, \quad (2)$$

where  $\frac{dCH_4^{OHloss}}{dt} = -k[OH][CH_4^{VMR}]$ ,  $CH_4^{VMR}$  is the zonal mean CH<sub>4</sub><sup>VMR</sup>,  $[OH]$  is the zonal mean boundary layer OH concentration and  $k$  is the reaction rate constant between CH<sub>4</sub> and OH.

Figure 2 shows the CH<sub>4</sub> column peak-to-peak amplitude due to seasonal changes in OH oxidation expressed as a percentage of the peak-to-peak amplitude of column CH<sub>4</sub>. As described in the main text, variations in column CH<sub>4</sub> due to OH are typically less than 10% of the column variation. This illustrative calculation is supported by the GEOS-Chem calculations described above.

## 1.7 Gridding data spatially and temporally

The two-dimensional fields of CH<sub>4</sub>,  $\Gamma$  and  $T_s$  were evaluated on a common 3° × 3° grid between 88.5°S to 88.5°N and 178.5°W to 178.5°E. The datasets are averaged at a temporal resolution of 10 days: the centre days chosen when GRACE data was available. The gridded data provides a global field for each parameter at each sampling point in time. We average all CH<sub>4</sub> measurements at a single grid-point within a certain time frame to create a 3° × 3° CH<sub>4</sub> field at each timestep. Due to the uneven coverage of SCIAMACHY data, as described above, the fields often have substantial gaps.

## 1.8 Seasonal de-trending

We remove the seasonal cycle from each time series by fitting a fixed period sine curve,  $A \sin(2\pi t_{years} + \phi)$ , allowing us to examine the seasonally independent relationship between these quantities. The seasonal de-trending experiments (Figure 3) show a significant correlation between the de-trended time series of CH<sub>4</sub> and temperature/gravity. We can therefore exclude the possibility of coincident seasonal variations between CH<sub>4</sub> and  $\Gamma$  or  $T_s$  as the main contribution of the correlations reported in the main paper.

## 1.9 River basin timeseries

100 We use geographical river basin boundaries (19) in order to examine the overall variations in  $\text{CH}_4$ ,  $\Gamma$  and  $T_s$  associated with 30 major river catchment areas. For each timestep we derive the mean  $\text{CH}_4$ ,  $\Gamma$  and  $T_s$ . Correlations between  $\text{CH}_4$ ,  $\Gamma$  and  $T_s$  are shown in Figure 4.

## 1.10 The InterTropical Convergence Zone and $\text{CH}_4$ columns over South America

105 The ITCZ refers to a region where Northeast and Southeast trade winds converge, resulting in upward motion of air and elevated precipitation. The ITCZ is typically between  $5^\circ$  N and  $5^\circ$  S but meanders on a seasonal scale, sometimes reaching midlatitudes. The ITCZ is an effective barrier for atmospheric mixing between North and South hemisphere.

In the main text, we suggest that the seasonal meandering of the ITCZ might help explain the weak relationship between variations of  $\text{CH}_4$  column and  $\Gamma$  over the Amazon basin. During Austral summer, the ITCZ shifts southward over South America which is accompanied by increased precipitation and higher  $\text{CH}_4$  concentrations, characteristic of the northern hemisphere. Increased precipitation will lead to an increase in  $\Gamma$ . We acknowledge that a sudden increase in  $\Gamma$  will not instantaneously increase  $\text{CH}_4$  emissions: water represents a barrier to  $\text{CH}_4$  diffusion from the soil to the atmosphere (due to the low solubility of  $\text{CH}_4$ ). Instead, we expect that  $\text{CH}_4$  emissions (and subsequent changes to the atmospheric column) will lag the initial flooding event as anaerobic conditions prevail in the soils and soil  $\text{CH}_4$  concentrations build up. Similarly, as the water table decreases we expect a peak in  $\text{CH}_4$  soil emission as the diffusion barrier is removed but the methanogenesis conditions continue. The spaceborne columns over South America represent a superposition of (a) the increase of atmospheric  $\text{CH}_4$  due to the southward migration of the ITCZ and (b) the increase in  $\text{CH}_4$  wetland emissions due to elevated precipitation (and a subsequent increase in  $\Gamma$ ) from the presence of the ITCZ. We also acknowledge that the elevated cloud cover associated with the ITCZ will reduce the sampling of this region during the wet season.

## 1.11 Gravity-temperature methanogenesis dependence

To determine the magnitude of wetland methanogenesis from SCIAMACHY  $\text{CH}_4^{VMR}$  columns we use equation 3 to describe global wetland methanogenesis (20):

$$F_{CH_4}^w = k_{CH_4} f_w C_s Q_{10}(T) \frac{T-T_0}{10}, \quad (3)$$

where  $C_s$  is soil carbon,  $f_w$  is the wetland cover fraction,  $T$  is the temperature averaged over some depth (K),  $T_0$  is 273.16 K,  $Q_{10}(T)$  is the methanogenesis temperature dependence, and  $k_{CH_4}$  is a calibration constant that ensures the required global emission budget. The value of  $Q_{10}(T)$  is dependent on the temperature range so a temperature independent constant  $Q_{10}(T_0)$  can be used to define the temperature sensitivity globally (20):

$$Q_{10}(T_0) = Q_{10}(T) \frac{T_0}{T}. \quad (4)$$

We adapt equation 3 to describe wetland emissions as a function of  $\Gamma$  and surface temperature:

$$F_{CH_4}^{w,\Gamma}(t) = k(D + \alpha\Gamma(t))Q_{10}(T)^{\frac{T(t)-T_0}{10}}, \quad (5)$$

where  $D$  is the initial volume of the water column;  $\Gamma(t)$  is the water column height change over time  $t$ ;  $\alpha$ , a coefficient between  $0 < \alpha < 1$ , indicates the fraction of  $\Gamma(t)$  affecting the wetland water volume; and  $k$  is a constant which absorbs  $C_s$  and  $f_w$  from equation 3. After factorising  $\alpha$  we normalise  $F_{CH_4}^{w,\Gamma}$  by adjusting  $k$  accordingly.

We define the  $CH_4$  column VMR at a surface location at time  $t$  as follows:

$$CH_4^{CVMR}(t) = \gamma F_{CH_4}^{w,\Gamma}(t) + S(t) + c \quad (6)$$

where  $F_{CH_4}^{w,\Gamma}(t)$  is the normalised local wetland  $CH_4$  emission;  $\gamma$  is the forward model that describes the relationship between emissions and observed column concentrations;  $S$  includes the remaining sources and sinks (including advection); and  $c$  is the background  $CH_4$  level. We assume zero covariance between  $F_{CH_4}^{w,\Gamma}$  and  $S$ , allowing us to solve equation 6 as a linear equation:

$$CH_4^{CVMR} = \gamma F_{CH_4}^{w,\Gamma}(t) + C, \quad (7)$$

where  $\gamma$  is the gradient, and the intercept  $C = (\bar{S} + c)$  is the sum of the remaining sources and sinks. In reality we expect some correlation between  $S$  and  $F_{CH_4}^{w,\Gamma}$ : a positive correlation would coincide in an overestimate of  $\gamma$ , and vice versa. Using equation 7, we solve for  $\frac{D}{\alpha}$  per grid square and  $Q_{10}(T)$  globally in order to maximise the correlation between  $F_{CH_4}^{w,\Gamma}$  and  $CH_4^{CVMR}$ . We exclude oceans, deserts and regions of permanent ice cover.

Equation 7 implies that where  $F_{CH_4}^{w,\Gamma}$  is zero the mean atmospheric concentration of  $CH_4$  is  $C$ , as expected. The wetland contribution to the atmospheric concentration is then:

$$\overline{CH_4^{CVMR}} - C = \overline{\gamma F_{CH_4}^{w,\Gamma}}. \quad (8)$$

Because  $\overline{F_{CH_4}^{w,\Gamma}} = 1$  the wetland contribution to the atmospheric concentration is equal to  $\gamma$ , which is the gradient between  $F_{CH_4}^{w,\Gamma}$  and  $CH_4^{CVMR}$ .

Finally, we scale the spatial distribution of  $\gamma$  ( $3^\circ \times 3^\circ$  resolution) to a global wetland+rice  $CH_4$  source of  $227 \text{ Tg y}^{-1}$  (21), with a resulting distribution in  $\text{mg m}^{-2} \text{ day}^{-1}$ . Oceans, deserts and regions with permanent ice cover are excluded from our global wetland analysis. We also exclude areas with negative correlations between  $F_{CH_4}^{w,\Gamma}$  and  $CH_4$ , but these represent only a small fraction of scenes.

## 1.12 $CH_4$ wetland emissions uncertainties

To obtain uncertainties for our wetland emission estimates of  $CH_4$  we propagate systematic errors associated with the method and random errors associated with the GRACE and NCEP/NCAR data. Figure 5 shows the sum of random and systematic uncertainties for the normalised wetland  $CH_4$  emission, representing c15–20% uncertainty globally and c40% over the tropics. Figure 3c from the main paper shows the uncertainty associated with the change in our wetland emission estimates relative to 2003 and so will only include the random errors.

The method includes fitting a wetland emission model to observed  $\text{CH}_4$  column from the SCIAMACHY instrument. We account for the uncertainty of  $\text{CH}_4^{CVMR}$  (ppb) using equation 1, using the mean fitting uncertainties for  $\text{CH}_4$  and  $\text{CO}_2$  column densities (molec/cm<sup>2</sup>) during 2003, and estimating an uncertainty of 1% for CarbonTracker  $\text{CO}_2$  concentrations (ppb). We also propagate uncertainty resulting from the linear fit of  $F_{\text{CH}_4}^{w,\Gamma}$  to  $\text{CH}_4^{CVMR}$  ( $\gamma$ ) using a two-step approach. First, by quantifying the error on linear fit per gridpoint and then quantifying the standard error of the mean statistics of the locally-fitted  $\gamma$  and its uncertainty. Using the GEOS-Chem chemistry transport model (see above) we estimate that the uncertainty of the global  $\gamma$  to be 16% (0.3/1.9).

The main sources of random error are GRACE measurements of  $\Gamma$  and NCEP/NCAR surface skin temperature. Uncertainties in GRACE measurements are within the range of 3–6mm (8). We assume a global mean uncertainty of 0.5 K for a 10-day mean of surface skin temperature, which is likely to be an overestimate. Total random errors correspond to 0.5 Tg/yr.

### 1.13 $\text{CH}_4$ wetland emissions over northern high latitudes

In the main paper we report  $\text{CH}_4$  wetlands emissions of  $4.2 \pm 1.0$  Tg from Arctic latitudes, defined here as  $>67^\circ$  N, which is smaller than the 10 Tg reported by another bottom-up inventory (22). We report in Table 1 our results in a manner consistent with other bottom-up wetland emission estimates at high northern latitudes. Generally, our results agree better with more recent studies.

Table 1: Wetland emission estimates at northern high latitudes from bottom-up inventories and our study.

Latitude region	Our Study [Tg]	Previous Studies [Tg]
40–80°N	$49 \pm 0.6$	47 (23)
50–70°N	$27 \pm 0.5$	62 (22)
$>66^\circ$ N	$3 \pm 0.2$	10 (22)
$>50^\circ$ N	$28 \pm 0.5$	45–106 (24)
$>45^\circ$ N	$41 \pm 0.6$	38 (25)
$>40^\circ$ N	$49 \pm 0.5$	31 (26)
$>30^\circ$ N	$68 \pm 0.8$	65 (27)

### 1.14 Wetland $\text{CH}_4$ emissions change between 2003–2007

To model changes in  $\text{CH}_4$  emissions over 2003–2007, we drive the wetland emission model adapted in this work and fitted for 2003–2005 (equation 5) with GRACE equivalent water height,  $\Gamma$ , and NCEP surface temperatures over that time period. We drive the model at a one-day temporal resolution in order to avoid seasonal bias due to missing data. To fill in the gap in GRACE data during January–March 2003 we use the adjusted seasonal equivalent for 2004.

We use 2003 as a baseline year and calculate the percentage increase in emission from the baseline. To determine the change in wetland emissions ( $\Delta$  Tg/y) we multiply the percentage increase to our estimated wetland emission distribution scaled by 170 Tg y<sup>-1</sup>, the median of bottom-up wetland emission estimates (21).

We use the GEOS-Chem chemistry transport model (described above), driven by a) our wetland  
175 emissions and b) a bottom-up inventory (15), to reproduce the observed CH<sub>4</sub> anomalies from surface  
flask sites (28–30) during 2003–2007. We define the anomaly as the long-term mean for each dataset  
subtracted from the dataset. Figure 6 shows that the magnitude and variability of CH<sub>4</sub> mole fraction  
anomalies (ppb) determined using our emission model are more consistent with the observations  
180 than the model using the bottom-up inventory. Our emission model is able to capture the positive  
anomaly since 2006 in both the northern and southern hemisphere (28–30), suggesting that changes  
in wetland emissions are partially responsible for recent changes in the global mean concentration  
of CH<sub>4</sub>.

## 2 Figures

### 2.1 Figure 1

185 Correlations ( $r^2$ ) between daily GEOS-Chem CH<sub>4</sub> columns (Jan-Dec, 2003), convolved with a mean  
SCIAMACHY averaging kernel, and the associated (top) rice paddy and (bottom) wetland CH<sub>4</sub>  
emissions.

### 2.2 Figure 2

190 Fractional contribution of CH<sub>4</sub> column variability due to variability in the OH sink, expressed as  
the ratio between the CH<sub>4</sub> column peak-to-peak amplitude due to seasonal changes in OH and the  
peak-to-peak amplitude of column CH<sub>4</sub>.

### 2.3 Figure 3

195 (Top) Signed correlation ( $r^2$ ) between the seasonally de-trended water table depth  $\Gamma$  (metres) and  
CH<sub>4</sub> concentration (ppb) during 2003-2005. A best-fit one-year period sine curve was used to remove  
the seasonal trend from both quantities. (Bottom) Signed correlation between the seasonally de-  
trended temperature and CH<sub>4</sub> concentration time series during 2003-2005 at each point. A best-fit  
one-year period sine curve was used to remove the seasonal trend from both quantities. Note the  
difference in scale from Figure 1 of main paper.

### 2.4 Figure 4

200 Signed correlation ( $r^2$ ) between CH<sub>4</sub> and groundwater (a) and temperature (b) over major river  
basins. River basin masks (19) are used as averaging windows for the CH<sub>4</sub> and groundwater data.  
Note the difference in scale from Figure 1 of main paper.



## 2.5 Figure 5

Uncertainties calculated for normalised CH<sub>4</sub> wetland emissions, shown in daily fluxes of CH<sub>4</sub> per unit area. An global uncertainty of 1% was used for CO<sub>2</sub> Carbon Tracker Data. Regions of large  
205 uncertainties mostly coincide with large CH<sub>4</sub> wetland emissions (see paper).

## 2.6 Figure 6

Monthly mean observed and model CH<sub>4</sub> mole fraction anomalies at northern (top) and southern hemisphere (bottom) surface measurement sites, 2003–2008 (28–30). Anomalies are calculated by  
210 subtracting the 2003–2008 mean concentration from the mole fraction timeseries. The GEOS-Chem chemistry transport model, driven by our wetland emissions (red) and a bottom-up emission inventory (blue) (15). Correlation ( $r$ ) between observed and model anomalies are shown inset.

## References

1. H. Bovensmann, *et al.*, *Journal of Atmospheric Sciences* **56**, 127 (1999).
- 205 2. C. Frankenberg, *et al.*, *Atmospheric Chemistry & Physics* **8**, 5061 (2008).
3. C. Frankenberg, *et al.*, *Geophysical Research Letters* **35**, L15811 (2008).
4. M. Buchwitz, *et al.*, *Atmospheric Chemistry & Physics* **5**, 941 (2005).
5. W. Peters, *et al.*, *Proc. Nat. Acad. Sci. USA* **104**, 18925 (2007).
6. B. D. Tapley, S. Bettadpur, J. C. Ries, P. F. Thompson, M. M. Watkins, *Science* **305**, 503  
220 (2004).
7. D. D. Rowlands, *et al.*, *Geophysical Research Letters* **32**, 4310 (2005).
8. J.-M. Lemoine, *et al.*, *Advances in Space Research* **39**, 1620 (2007).
9. E. Kalnay, *et al.*, *Bulletin of the American Meteorological Society* **77**, 437 (1996).
10. M. E. Mann, G. A. Schmidt, *EGS - AGU - EUG Joint Assembly, Abstracts from the meeting  
225 held in Nice, France, 6 - 11 April 2003, abstract #1574* pp. 1574+ (2003).
11. B.-J. Tsuang, M.-D. Chou, Y. Zhang, A. Roesch, K. Yang, *J. Climate* **21** (2008).  
Doi:10.1175/2007JCLI1502.1.
12. J. G. J. Olivier, J. A. V. Aardenne, F. Dentener, L. Ganzeveld, J. A. H. W. Peters, *Non-  
CO2 Greenhouse Gases (NCGG-4)* (Millpress, Rotterdam, 2005), chap. Recent trends in global  
230 greenhouse gas emissions: regional trends and spatial distribution of key sources, pp. 325–330.  
ISBN 90 5966 043 9.
13. G. R. van der Werf, *et al.*, *Atmospheric Chemistry & Physics* **6**, 3423 (2006).

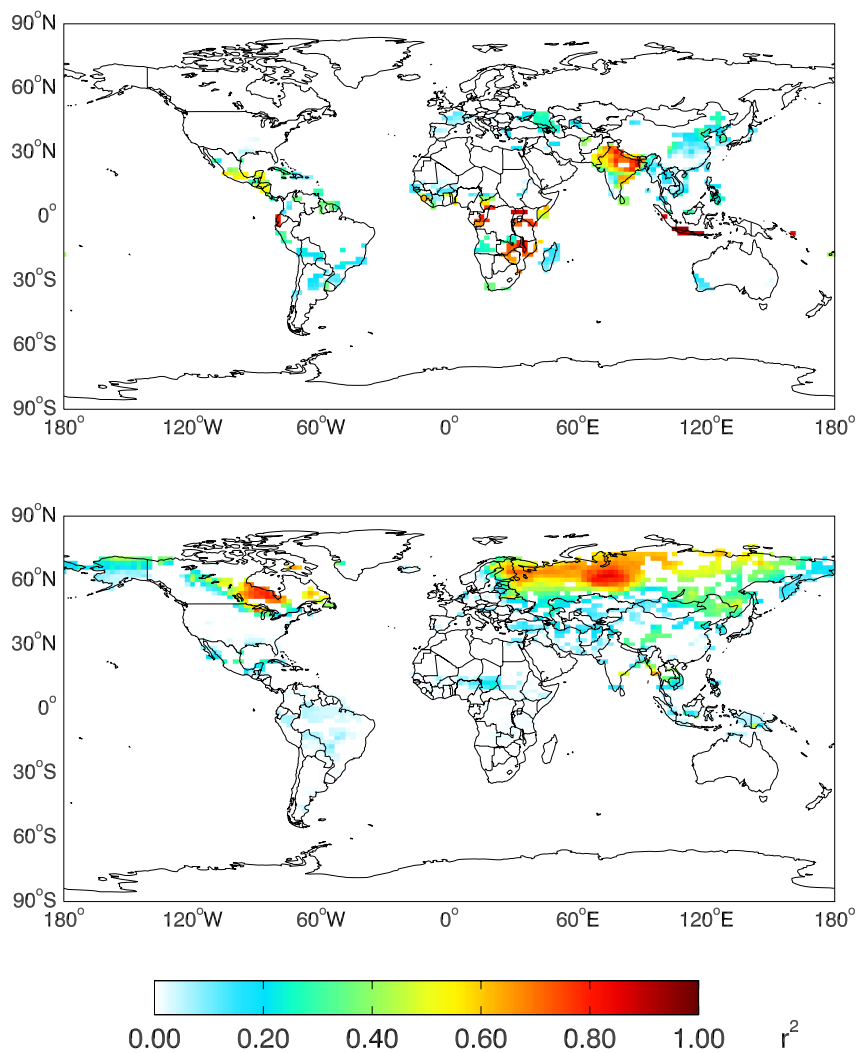


Figure 1: Correlations ( $r^2$ ) between daily GEOS-Chem CH<sub>4</sub> columns (Jan-Dec, 2003), convolved with a mean SCIAMACHY averaging kernel, and the associated (top) rice paddy and (bottom) wetland CH<sub>4</sub> emissions.

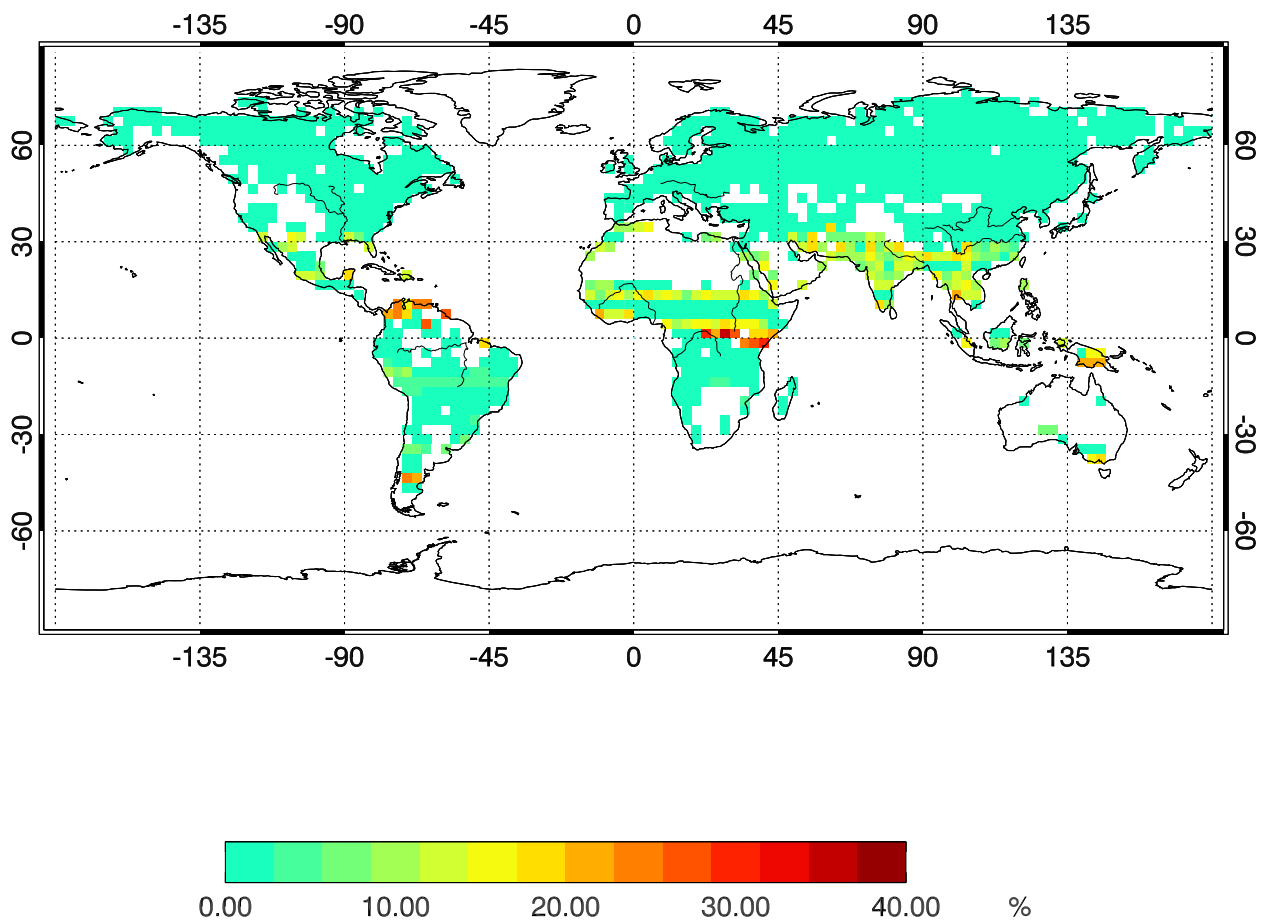


Figure 2: Fractional contribution of  $\text{CH}_4$  column variability due to variability in the OH sink, expressed as the ratio between the  $\text{CH}_4$  column peak-to-peak amplitude due to seasonal changes in OH and the peak-to-peak amplitude of column  $\text{CH}_4$ .

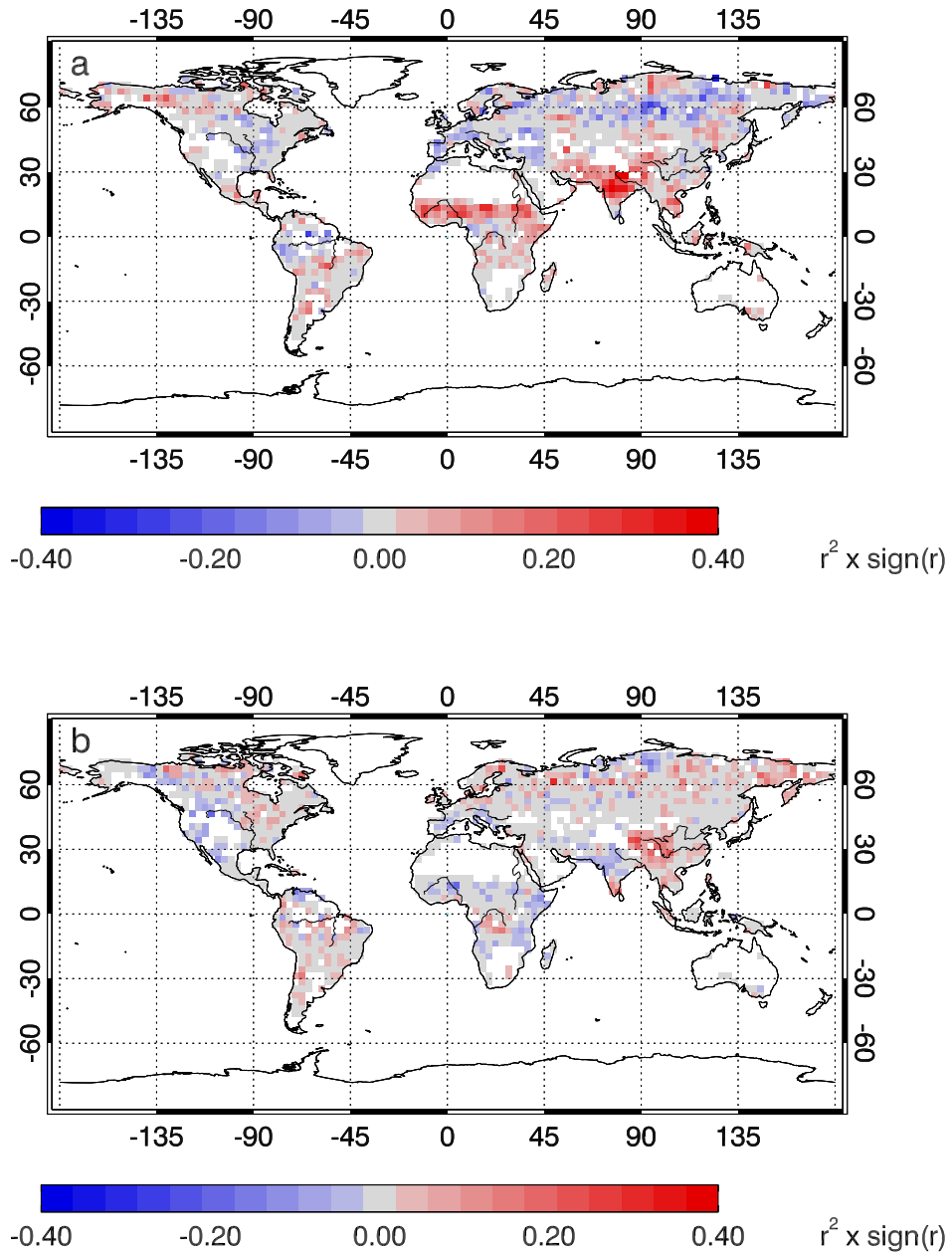


Figure 3: (Top) Signed correlation ( $r^2$ ) between the seasonally de-trended water table depth  $\Gamma$  (metres) and  $\text{CH}_4$  concentration (ppb) during 2003-2005. A best-fit one-year period sine curve was used to remove the seasonal trend from both quantities. (Bottom) Signed correlation ( $r^2$ ) between the seasonally de-trended temperature and  $\text{CH}_4$  concentration time series during 2003-2005 at each point. A best-fit one-year period sine curve was used to remove the seasonal trend from both quantities. Note the difference in scale from Figure 1 of main paper.

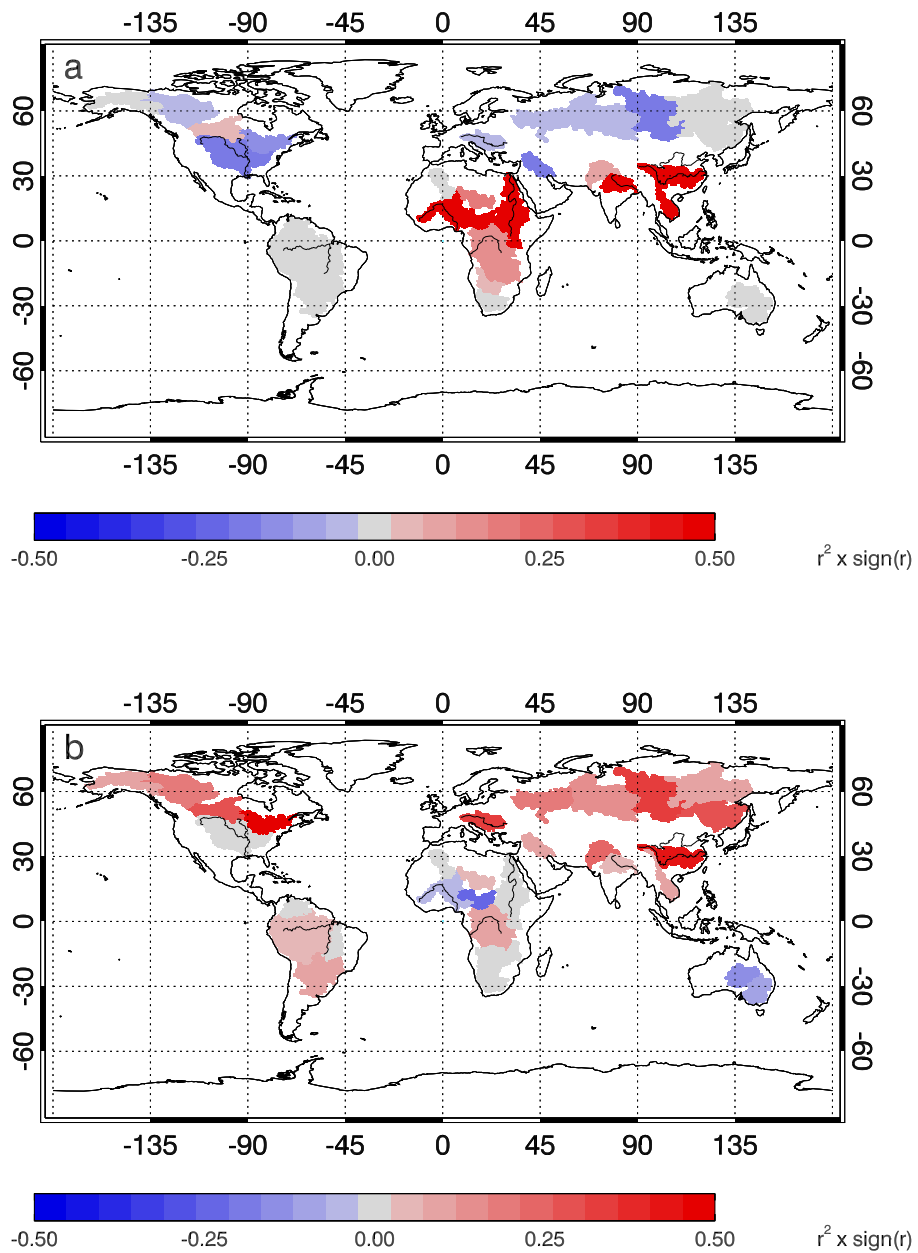


Figure 4: Signed correlation ( $r^2$ ) between  $\text{CH}_4$  and groundwater (a) and temperature (b) over major river basins. River basin masks (19) are used as averaging windows for the  $\text{CH}_4$  and groundwater data. Note the difference in scale from Figure 1 of main paper.

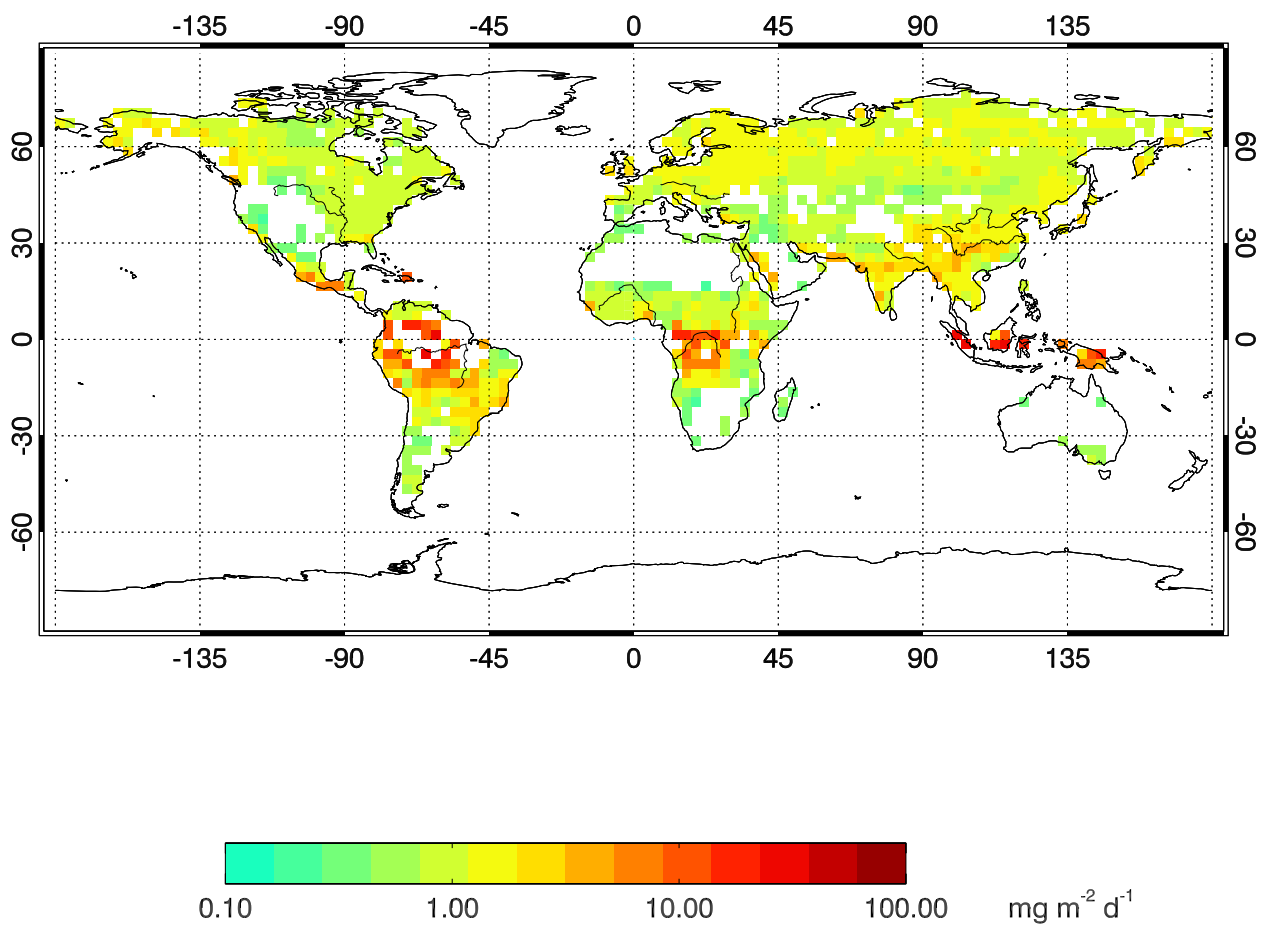


Figure 5: Uncertainties calculated for normalised CH<sub>4</sub> wetland emissions (see text), expressed as daily fluxes of CH<sub>4</sub> per unit area ( $\text{mg m}^{-2} \text{d}^{-1}$ ).

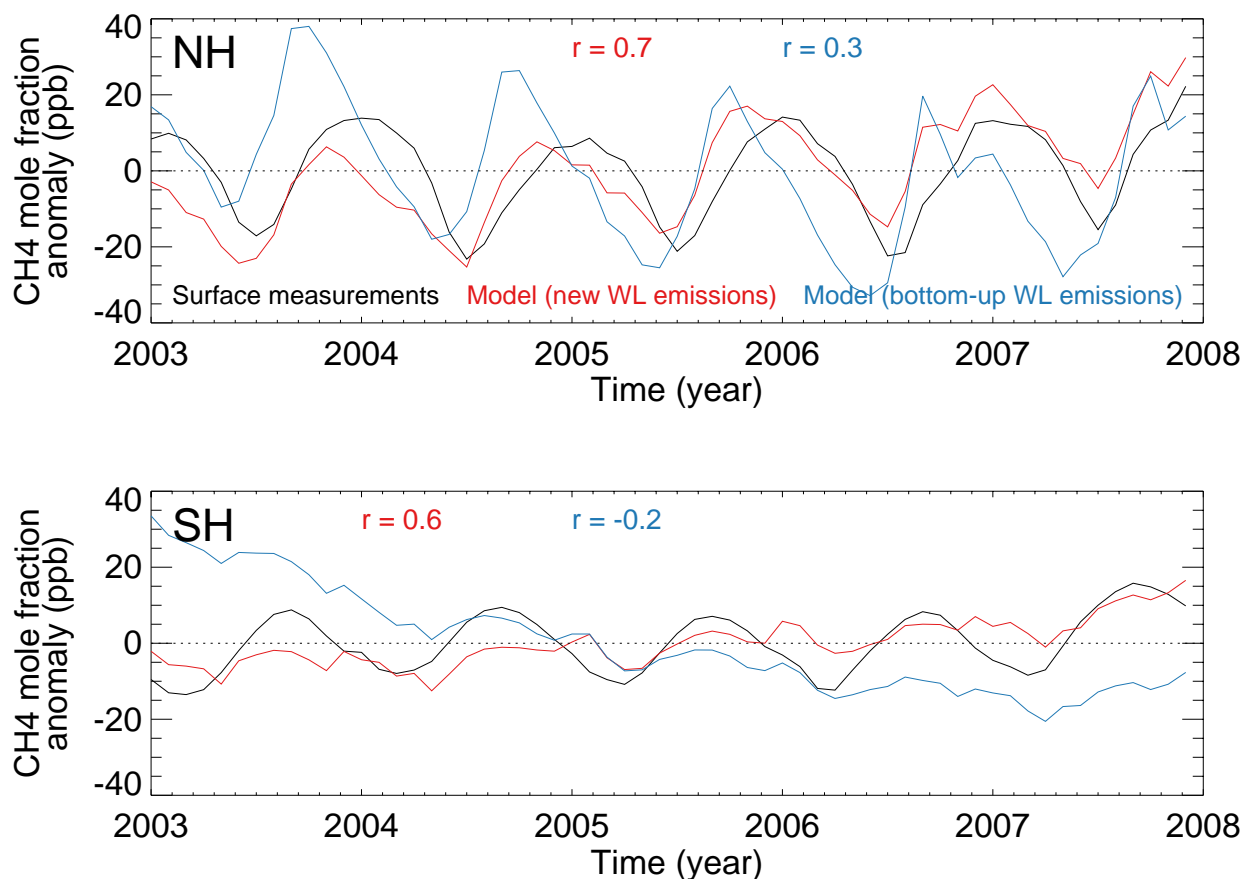


Figure 6: Monthly mean observed and model CH<sub>4</sub> mole fraction anomalies at northern (top) and southern hemisphere (bottom) surface measurement sites, 2003–2008 (28–30). Anomalies are calculated by subtracting the 2003–2008 mean concentration from the mole fraction timeseries. The GEOS-Chem chemistry transport model, driven by our wetland emissions (red) and a bottom-up emission inventory (blue) (15). Correlation ( $r$ ) between observed and model anomalies are shown inset.

14. B. N. Duncan, R. V. Martin, A. C. Staudt, R. Yevich, J. A. Logan, *J. Geophys. Res* **108** (2003).  
Doi:10.1029/2002JD002378.
- 235 15. I. Fung, *et al.*, *Journal of Geophysical Research* **96**, 13033 (1991).
16. A. Fiore, *et al.*, *Journal of Geophysical Research (Atmospheres)* **108**, 4787 (2003).
17. J. S. Wang, *et al.*, *Global. Biogeochem. Cycles* **18** (2004). Doi:10.1029/2003GB002180.
18. D. York, N. M. Evensen, M. Lopez-Martinez, J. D. B. Delgado, *Am. J. Phys.* **72**, 367 (2004).
19. T. Oki, Y. C. Sud, *Earth Interactions* **2**, 1 (1998).
- 240 20. N. Gedney, P. M. Cox, C. Huntingford, *Geophysical Research Letters* **31**, 20503 (2004).
21. K. Denman, *et al.*, *Couplings Between Changes in the Climate System and Biogeochemistry. In: Climate Change 2007: The Physical Science Basis. Contribution of Working Group I to the Fourth Assessment Report of the Intergovernmental Panel on Climate Change [Solomon, S., D. Qin, M. Manning, Z. Chen, M. Marquis, K.B. Averyt, M. Tignor and H.L. Miller (eds.)].*  
245 (Cambridge University Press, Cambridge, United Kingdom and New York, NY, USA., 2007).
22. E. Matthews, I. Fung, *Global Biochemical Cycles* **1**, 61 (1987).
23. Y. Liu, Modeling the emissions of nitrous oxide (N<sub>2</sub>O) and methane (CH<sub>4</sub>) from the terrestrial biosphere to the atmosphere, Ph.D. thesis, MIT (1996).
24. D. I. Sebacher, R. C. Harriss, K. B. Bartlett, S. M. Sebacher, S. S. Grice, *Tellus Series B  
250 Chemical and Physical Meteorology B* **38**, 1 (1986).
25. K. B. Bartlett, R. C. Harriss, *Chemosphere* **26**, 261 (1993).
26. C. Mingkui, K. Gregson, S. Marshall, *Atmospheric Environment* **32**, 3293 (1998).
27. B. P. Walter, M. Heimann, E. Matthews, *Journal of Geophysical Research* **106**, 34189 (2001).
28. R. G. Prinn, *et al.*, *J. Geophys. Res.* **105**, 17751 (2000).
- 255 29. E. J. Dlugokencky, P. Lang, K. Masarie, Atmospheric methane dry air mole fractions from the NOAA ESRL carbon cycle cooperative global air sampling network, 1983-2007, version: 2008-07-02 (2009). Ftp://ftp.cmdl.noaa.gov/ccg/ch4/flask/event/.
30. R. L. Francey, *et al.*, Global atmospheric sampling laboratory (GASLAB): supporting and extending the Cape Grim trace gas programs. baseline atmospheric program (Australia) 1993  
260 (1996). Edited by R.J. Francey, A.L. Dick and N. Derek, pp 8-29, Bureau of Meteorology and CSIRO Division of Atmospheric Research, Melbourne, Australia.